II   Theory

The kinematics of the electron-induced three-body breakup reaction of
^{3}He and the relevant physics observables are discussed. Interpretation
of the measured cross sections requires comparison with predictions of
a theoretical model. In this chapter, the model developed by Golak *et
al.* [Gol95] is introduced and the procedure developed to compare results
of this model to data is detailed.

2.1   Kinematics of electron-induced ^{3}He breakup

In the exclusive electron-induced two-nucleon knockout reaction, energy and
momentum are transferred to a nucleus by a virtual photon. After the reac-
tion the momenta of the scattered electron and the emitted nucleons are deter-
mined. The remainder of the nucleus is left intact and no secondary particles
are created. This reaction mechanism is schematically shown in Fig. 2.1. The
energy transfer ω and three-momentum transfer $\boldsymbol{q}$ is calculated from the mo-
mentum difference between the incoming and scattered electron. If the electron
mass is neglected, as it is much smaller than its energy E, then we can define
$\omega \equiv E_e - E_{e'} = c(p_e - p_{e'})$ and $\boldsymbol{q} = \boldsymbol{p}_e - \boldsymbol{p}_{e'}$.

In the present ^{3}He$(e, e'pp)$ experiment the two protons, with momenta $\boldsymbol{p}_1'$
and $\boldsymbol{p}_2'$, resulting from the full breakup of ^{3}He are detected. As no particles
are created, the final state can be reconstructed completely and the missing
momentum $\boldsymbol{p}_m = \boldsymbol{q} - \boldsymbol{p}_1' - \boldsymbol{p}_2'$ can be identified with the momentum of the
undetected neutron $\boldsymbol{p}_3'$. Energy conservation requires the missing energy E_m to
be equal to the binding energy E_b of the ^{3}He nucleus: $E_m = \omega - T_1 - T_2 -
T_{rec} = E_b$, where T_{rec} is the kinetic energy of the recoiling neutron, which can
be calculated from $\boldsymbol{p}_m$, T_1 and T_2 being the kinetic energies of the two emitted
protons. The binding energy of ^{3}He is 7.718 MeV [Til87].

As the direction of the virtual-photon momentum defines a natural direction
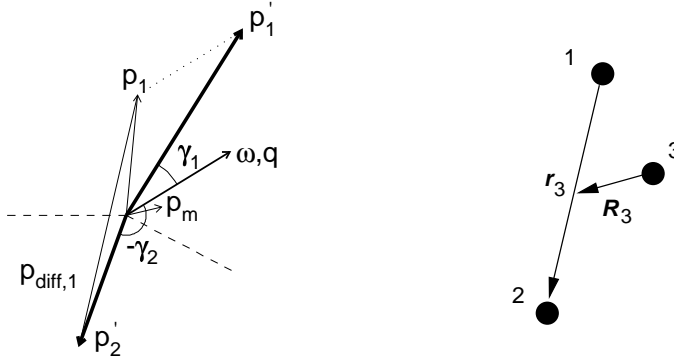of preference, it is convenient to describe the scattering process in a coordinate

Figure 2.1: *Kinematic configuration of an $(e, e'pp)$ reaction. For clarity, the momentum vectors are shown all in one plane. The dashed lines represent the incoming and scattered electron; the bold vectors detected protons and the thin vectors derived quantities. Coupling of the photon to proton–1 has been assumed. The right-hand figure shows the Jacobi coordinates in the three-body system.*

system in which a vector $\boldsymbol{p}$ is expressed as $\boldsymbol{p} = (p, \gamma, \zeta)$, where γ represents the polar angle between the momentum of the particle and the momentum transfer $\boldsymbol{q}$. The angle ζ is defined as the angle between the electron scattering plane and the plane containing both $\boldsymbol{p}$ and $\boldsymbol{q}$. For clarity the prime is dropped from the angles γ and ζ; hence, γ_1 is the angle between $\boldsymbol{q}$ and $\boldsymbol{p}_1'$. For convenience, proton–1, of which the momentum vector has the smallest angle with respect to $\boldsymbol{q}$, is labelled 'forward', and the second proton 'backward'.

In the description of three-body kinematics Jacobi coordinates are introduced as $\boldsymbol{r}_k = \boldsymbol{x}_i - \boldsymbol{x}_j$ and $\boldsymbol{R}_k = \boldsymbol{x}_k - \frac{1}{2}(\boldsymbol{x}_i + \boldsymbol{x}_j)$ as shown in Fig. 2.1 [Glö83]. The indices ijk are cyclic permutations of the particle indices 1, 2, and 3. The corresponding Jacobi momenta are then defined as[*]:

$$\boldsymbol{p}_{rel,k} = \tfrac{1}{2}(\boldsymbol{p}_i - \boldsymbol{p}_j) \quad \text{and} \quad \boldsymbol{p}_{cm,k} = \tfrac{2}{3}[\boldsymbol{p}_k - \tfrac{1}{2}(\boldsymbol{p}_i + \boldsymbol{p}_j)]. \tag{2.1}$$

[*]The Jacobi momenta are usually called $\boldsymbol{p}$ and $\boldsymbol{q}$, as in Ref. [Glö83]. To avoid ambiguity between the individual nucleon momenta, the three-momentum transfer and the Jacobi momenta, they are here labelled $(\boldsymbol{p}_{rel}, \boldsymbol{p}_{cm})$.

2.2   Breakup of ^{3}He by an electromagnetic probe

The interaction of an electron with ^{3}He can well be described within the one-photon exchange approximation. In this case the differential cross section for full breakup of the tri-nucleon system, in absence of spin observables, is written as

$$d\sigma^{3N}\rfloor_{lab} = \frac{1}{(2\pi)^2}\frac{E'}{E}m_e^2|M_{fi}^{3N}|^2\delta(M_t+\omega-E_1'-E_2'-E_3')\delta^3(\boldsymbol{q}-\boldsymbol{p}_1'-\boldsymbol{p}_2'-\boldsymbol{p}_3')$$

$$dE'd\Omega_e d^3\boldsymbol{p}_1' d^3\boldsymbol{p}_2' d^3\boldsymbol{p}_3', \quad (2.2)$$

where $m_e^2|M_{fi}^{3N}|^2$ is the contraction of the leptonic and hadronic tensor, the delta-functions take energy and momentum conservation into account, E is the total relativistic energy and m_e is the electron mass [Golth]. Integration over the momentum vector $\boldsymbol{p}_3'$ of the third, unobserved, particle and the momentum of the second particle p_2 yields the eight-fold differential cross section

$$\frac{d^8\sigma}{dE'd\Omega_{e'}dT_1'd\Omega_1 d\Omega_2} = \frac{1}{(2\pi)^2}\frac{E'}{E}\,m_e^2|M_{fi}^{3N}|^2\,\rho_f^{3N} \qquad (2.3)$$

where ρ_f^{3N} is the phase space factor

$$\rho_f^{3N} = \frac{E_1|\boldsymbol{p}_1'|\,\boldsymbol{p}_2'^{\,2}}{\left|\frac{|\boldsymbol{p}_2'|}{E_2}-\frac{\boldsymbol{p}_2'\cdot\boldsymbol{p}_3'}{|\boldsymbol{p}_2'|E_3}\right|}. \qquad (2.4)$$

The transition matrix element $|M_{fi}^{3N}|^2$ can be separated in a purely leptonic part and a sum over the product of kinematic factors and hadronic structure functions W. It can be shown on general grounds [Bof96] that in the case of two-nucleon knockout only six independent structure functions contribute to the unpolarized cross section:

$$m_e^2|M_{fi}|^2 = (2\pi)^2\frac{E}{E'}\sigma_{Mott}\sum_i v_i W_i, \qquad (2.5)$$

with (α being the finestructure constant)

$$\sigma_{Mott} = \frac{\alpha^2\cos^2\frac{\theta_{e'}}{2}}{4E^2\sin^4\frac{\theta_{e'}}{2}}. \qquad (2.6)$$

Four of the structure functions used in this framework are also present in single-nucleon knockout: W_C, W_T, W_I, and W_S as defined by De Forest [For83]. The
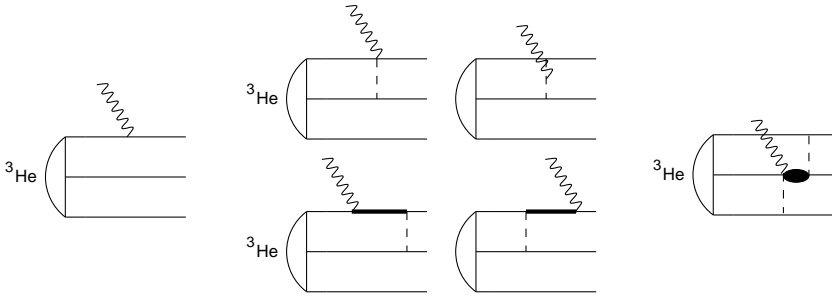
Figure 2.2: *Schematic representation of virtual-photon absorption by the* ^{3}He
*nucleus. The left-hand graph shows interaction via a one-body
hadronic current, the four graphs in the middle represent various
two-body mechanisms: coupling to mesons and intermediate Δ ex-
citation and de-excitation. An example of a three-body mechanism
is shown on the right; the shaded oval represents anything except a
nucleon.*

two additional structure functions contributing in $(e, e'pp)$ are arbitrarily labelled
X and Y by Golak [Golth].

The structure functions W are combinations of the nuclear matrix element
N^μ [Gol95],

$$N^\mu \equiv \langle \Psi_{scatt}^{(-)}(\boldsymbol{q}) | \hat{j}^\mu | \Psi_{bound}(\boldsymbol{P}) \rangle, \tag{2.7}$$

where $\Psi_{scatt}^{(-)}$ and Ψ_{bound} are fully antisymmetric solutions of the $3N$ scattering
state and the initial ^{3}He bound state, respectively. The nuclear current opera-
tor $\hat{j}^\mu$ describes the coupling of the virtual photon to this bound state, making
the transition to the scattering state $\Psi_{scatt}^{(-)}(\boldsymbol{q})$. In the initial state the total
momentum $\boldsymbol{P}$ is zero while the total momentum of the final state equals $\boldsymbol{q}$.

Photoabsorption mechanisms

There are various ways the virtual photon can couple to the ^{3}He nucleus, some
of which are depicted in Fig. 2.2.

The one-body hadronic current takes into account the absorption of a vir-
tual photon on one nucleon only, which subsequently leads to the full breakup
of the tri-nucleon system. In a non-relativistic reduction, the one-body hadronic

current consists of three parts: a charge-density operator, a convection current operator – which determines the orbital magnetic moment of the nucleons – and a spin current operator, which is associated with their spin magnetic moment [Golth].

Breakup of the ^{3}He nucleus can also occur via two-body hadronic currents, thus sharing both the energy and the momentum between the two nucleons. In the energy and momentum transfer domain under study, the relevant two-body currents are coupling of the virtual photon to mesons (meson-exchange currents or MECs) and excitation of the Δ resonance in an intermediate state (isobar currents or ICs). Their importance strongly depends on the isospin of the NN pair. In the case of a pp pair the contribution of MECs to the cross section will be strongly suppressed, as the virtual photon to first relativistic order does not couple to such a pair [Giu91]. Also the contribution due to isobar currents is reduced in case the two protons are in a relative $^1S_0$ state, as the transition via the resonant M1 multipole is forbidden by angular momentum and parity conservation rules. Therefore Δ excitation is only possible via the much weaker non-resonant E1 and E2 multipoles [Wilh96]. These restrictions on MECs and ICs are not applicable to pn pairs. It may therefore be expected that in a direct $(e, e'pp)$ reaction the influence of these two-body currents is reduced compared to the $(e, e'pn)$ case.

In addition, the photon can couple to all three particles by a three-body mechanism, *e.g.*, by coupling to the simultaneous exchange of two mesons. Sensitivity to these processes will exist at photon energies around 500–600 MeV and in specific regions of phase space, where the struck meson initially propagates on-shell and is subsequently reabsorbed by the remaining nucleon pair [Bof96].

Final-state rescattering

The interaction among the three nucleons in the final state (FSI), *i.e.*, after the interaction of the virtual photon with the tri-nucleon system, can strongly influence the cross section for specific kinematic configurations. It has been convincingly shown [Meij86, Ish94] that multiple rescattering among the outgoing nucleons leads to cross sections that are significantly different compared to those calculated in a plane-wave approach. Truncation to single-rescattering
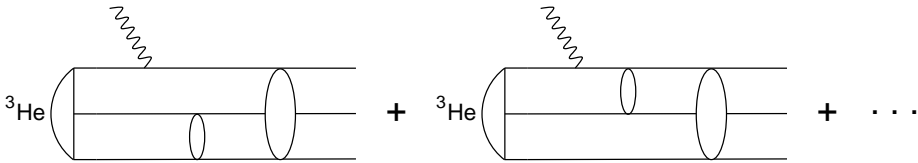
Figure 2.3: *Schematic representation of multiple-rescattering among the nucleons in the final state, following an interaction via a one-body hadronic current. The 'blobs' represent the 2N scattering operator (t-matrix).*

processes only is insufficient. A schematic representation of the rescattering process is given in Fig. 2.3.

2.3 Calculation of the breakup cross section

The differential cross section of the exclusive three-body breakup of the tri-nucleon system can be calculated by solving Faddeev-type equations for both the bound state and the final, 'scattering' state [Glö96, Meij86]. Alternatively, one can apply a diagrammatic approach, in which the presumably most important processes are added coherently [Lag87]. Whereas the diagrammatic approach allows inclusion of realistic two-body mechanisms, especially isobar currents, it is not suited to account for rescattering effects up to infinite order. As it has been shown in both theoretical [Meij86, Ish94] and experimental [Poo99] studies, that higher-order rescattering can have a significant effect, and calculations are available that include these processes [Gol95], the measured cross sections are compared to the results of these 'continuum Faddeev' calculations only. They are based on realistic models of the NN interaction that fit the NN scattering data with a χ^2 per datum of approximate one. In this section, the formalism employed to calculate the ^{3}He$(e, e'pp)$ cross section within this framework is reviewed.

Solving the three-body problem

The Faddeev decomposition of the Schrödinger equation provides a powerful tool to solve the three-body problem. In the presence of two-body interactions only,

the Schrödinger equation for the complete three-body wave function with merely pair interactions can be written as the sum of three similar equations that each involve only one pair interaction [Car98]. This method has been successfully applied to the ^{3}He bound-state for different types of NN interaction models, but is also suited for solving the scattering state of the three nucleons.

In the procedures used by Golak *et al.* [Gol95], the Faddeev equations are solved in momentum space. The initial ^{3}He bound state is solved and projected onto a basis $|p_{rel}p_{cm}\alpha\rangle$. The index α labels a partial wave or *channel, i.e.,* a unique combination of orbital angular momentum, spin and isospin quantum numbers of the nucleon pair and the spectator. In the calculation of the bound-state wave function, thirty-four channels are considered. The nuclear matrix element from Eq. (2.7) can subsequently be formally separated in two parts: *i)* N^μ_{PWIAS}, which is the transition matrix element between the initial bound state, the current operator and a fully symmetrized plane wave of three nucleons without any mutual interaction and *ii)* N^μ_{rescatt}, which includes all rescattering processes. To retain consistency with the calculated wave functions, the current operator $\hat{j}^\mu$ is used in a non-relativistic approximation [Ish94].

It should be noted that the final state obtained from N^μ_{PWIAS} consists of a symmetrized plane wave, which is no eigenstate of the $3N$ Hamiltonian and is non-orthogonal to the ^{3}He bound state. It can therefore not be compared to data and can only serve to illustrate the effect of ingredients in the calculation by comparing different PWIAS results.

The equation defining the rescattering matrix element N^μ_{rescatt} leads to a multiple-scattering series, involving the repeated application of the NN t-operator. It is derived from the solution of a Faddeev-like integral equation which sums up this multiple-scattering series [Gol95]. The solution of the integral equation depends only on the characteristics of the virtual photon involved, *i.e.,* (ω, q). A projection of this solution onto the basis $\langle p_{rel}p_{cm}\alpha|$ subsequently allows straightforward calculation of N^μ_{rescatt} for specific final states. In this way, the computationally most involved part – solving the integral equations – has to be performed only once for any given (ω, q) value [Gol95].

The sum of PWIAS and the rescattering contribution yields the complete solution of the nuclear matrix element N^μ.
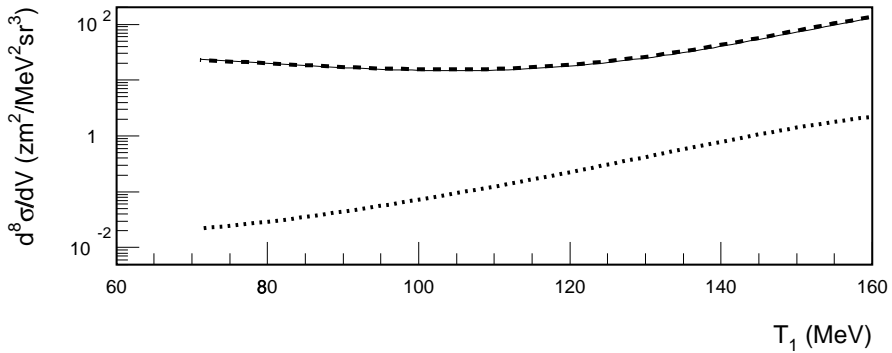
Figure 2.4: *Differential plane-wave cross section for various coupling mechanisms: coupling to the proton emitted in forward direction (dashed), coupling to the backward proton (dotted) and the coherent sum of coupling to particle 1, 2, and 3 (solid). Kinematic setting LQ, $\theta_1 = 54°$, $\theta_2 = -120°$.*

One-body currents and the bound-state wave-function

Information on the initial ^{3}He bound state can in principle be obtained from reactions induced by a one-body hadronic current; in this case, the momentum of the virtual photon is transferred to a single nucleon only. In absence of final-state rescattering, this implies for the non-struck particles that the momenta observed in the final state equal their initial-state values and that the exact initial-state configuration can be reconstructed. However, the information on which nucleon was hit cannot be reconstructed from the data as the measured cross section (even in the plane-wave impulse approximation, PWIAS) is the coherent sum of coupling to any of the three nucleons.

Insight in the coupling mechanism can been deduced from the PWIAS calculations of Golak *et al.*. Although their absolute magnitude cannot be compared to the experimental data they are nevertheless valuable to determine the relative importance of the coupling to the various particles leading to the same final state. Figure 2.4 shows the cross section for the ^{3}He$(e, e'pp)$ reaction for the central kinematic configuration of LQ (see section 3.6): over the entire energy
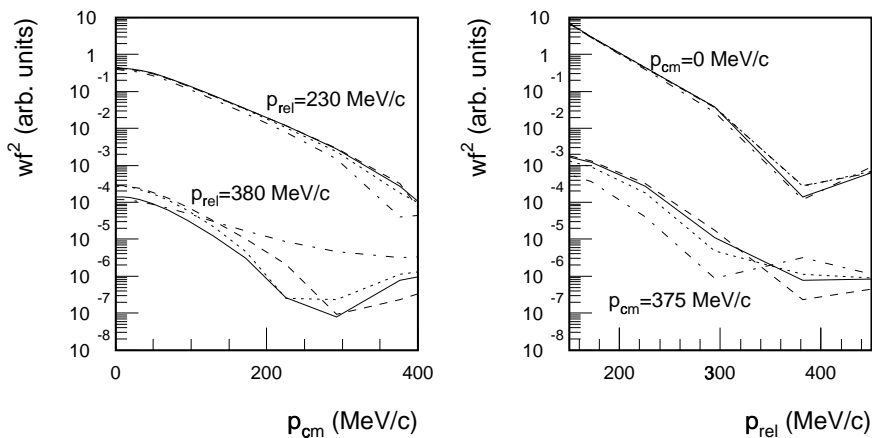
Figure 2.5: *Probability of the* ^{3}He *bound-state wave function for a two-nucleon system in a relative* $^1S_0$ *state. On the left-hand side as a function of the centre-of-mass momentum, on the right-hand side as a function of the relative momentum in the nucleon pair. The curves show calculations with the Bonn-B (solid), CD-Bonn (dashed), Nijmegen-93 (dotted) and Argonne v_{18} (dot-dashed) potential models.*

acceptance, the cross section is predicted to be dominated by coupling to the forward proton.

Once the coupling mechanism is known, the relative momentum inside the pp pair in the initial state can be determined. In absence of final state rescattering, the $(e, e'pp)$ reaction directly probes the initial ^{3}He wave function as shown in Fig. 2.5 for a nucleon pair in the $^1S_0$ state. The bound-state wave functions shown are based on Faddeev calculations performed with various models of the NN interaction: Bonn-B, charge-dependent Bonn (CD-Bonn), Nijmegen-93 and Argonne v_{18}. The left panel shows the neutron momentum density distribution for two values of the NN-relative momentum. In kinematic setting LQ of the present experiment this relative momentum p_{rel} ranges from 210 to 350 MeV/c, if coupling of the photon to the forward proton is assumed. The right-hand panel shows a relative NN momentum density distribution for two values of the neutron momentum. At low values of the centre-of-mass and relative momentum the results obtained using the various potential models are similar. Only at high
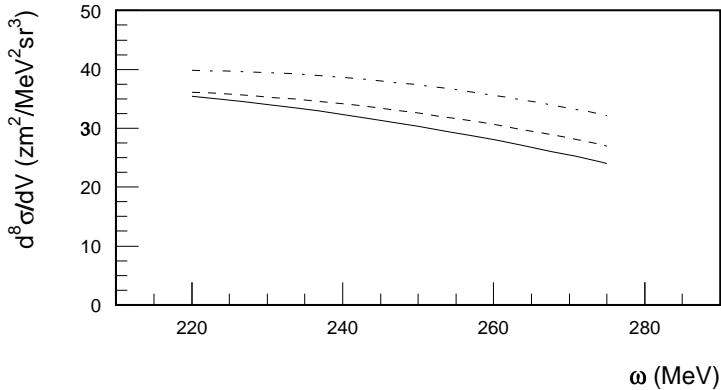
Figure 2.6: *Cross sections for the ^{3}He$(e, e'pp)$ reaction for varying energy trans-*
fer. The cross section was averaged over the acceptance of this ex-
periment and corresponds to situations where the neutron can be
considered as a spectator ($p_m = 30$ MeV/c). The solid, dashed and
dash-dotted curves correspond to calculations with only one-body,
with MEC and with MEC+Δ currents, respectively.

centre-of-mass or relative momentum differences can be observed that are due
to the potential model used.

Two-body currents

Two-body hadronic currents involve coupling of the virtual photon to exchanged
mesons, and excitation or de-excitation of Δ isobars. Meson-exchange currents
have been incorporated in the solution of the continuum Faddeev equations using
a formalism due to Schiavilla *et al.* [Sch89], which includes coupling to one-pion
and one-rho exchange. To incorporate these currents in a way compatible with
the potential model used, the exchange interactions are modified by multiplica-
tion with an additional form factor [Golpc].

A preliminary expression for the isobar currents [Sch89] was included in the
calculations in a similar way. The simplified expression for the $\pi\Delta$ current reads

$$\boldsymbol{j}_{\pi\Delta}(\boldsymbol{k}_1, \boldsymbol{k}_2) \propto \frac{1}{(m_\Delta - m_N)} \, G_M^V(q) \cdots, \tag{2.8}$$

where $G_M^V(q)$ is the isovector magnetic form factor and m_Δ the mass of the Δ_{33} resonance (the $\rho\Delta$ current is similar). The current includes terms for the excitation of a nucleon to a Δ isobar as well as terms that describe the de-excitation of a 'pre-existing' Δ to a nucleon by an electromagnetic interaction. The expression quoted, also known as the *static* Δ, does not depend on the energy transfer to the system and thus will not produce the required resonant behaviour, as is shown in Fig. 2.6. This formalism should therefore been seen as a first step towards incorporation of the Δ current. A more accurate treatment of isobar currents in the Faddeev calculations will be necessary before firm statements about the role of the Δ can be made.

2.4   Choice of observables

The cross section of the ${}^3\text{He}(e, e'pp)$ reaction depends on seven independent kinematic variables. However, the statistical accuracy of the data does not allow representation of the measured cross section for small intervals in all seven quantities simultaneously. The properties of the current operator and of the ${}^3\text{He}$ bound-state wave function suggest that a limited set of observables carries most of the information of the ${}^3\text{He}(e, e'pp)$ process.

The electron kinematics naturally defines two relevant observables: the energy transfer ω and the momentum transfer q. Alternatively, the energy transfer ω can be exchanged for the invariant energy $W_{N'N'}$ of two nucleons in the final state. The ${}^3\text{He}$ momentum distributions shown in Fig. 2.5 suggest an important role for the relative and pair momenta. Therefore, the missing momentum p_m, which in a direct $(e, e'pp)$ reaction mechanism reflects the neutron momentum in the initial state, is selected as an observable.

Investigation of the coupling mechanisms by one-body currents shows a dominant role for coupling of the virtual photon to the forward proton. In this case, the Jacobi momentum $\boldsymbol{p}_{rel,3}$ in the initial state can be related to the momentum

$$\boldsymbol{p}_{diff,1} = (\boldsymbol{p}_1' - \boldsymbol{q}) - \boldsymbol{p}_2' \triangleq \boldsymbol{p}_1 - \boldsymbol{p}_2 \equiv 2\boldsymbol{p}_{rel,3}. \tag{2.9}$$

Another significant process that influences the cross section is the rescattering among the outgoing nucleons. Especially when two nucleons are emitted with (vectorially) comparable momenta the cross section will be notably enhanced.

Within the experimental detection volume, such 'FSI configurations' occur between the forward proton and the unobserved neutron. Hence, the momentum difference of these two nucleons was selected as an observable:

$$\boldsymbol{p}_{ij} = \boldsymbol{p}'_i - \boldsymbol{p}'_j. \tag{2.10}$$

The 'FSI configuration' corresponds to $p_{ij} \rightarrow 0$ MeV/c.

2.5 Numerical results

Comparison of the theoretical model by Golak *et al.* to the data requires calculation of the cross section for specific kinematic configurations, as well as the evaluation and averaging of the cross section over the experimental detection volume. In this section the methods employed and their associated uncertainties are discussed.

Uncertainties within the theoretical model

For computational reasons not all components of the NN interaction are taken into account in the calculations. The number of relevant components depends on the kinematic conditions of the reaction. In general, a higher energy and momentum transfer implies that more force components should be taken into account.

In view of the uncertainties associated with the measured cross section, a 'theoretical' accuracy of approximately 10% should be aimed at. To determine the uncertainty associated with the choice for $j \leq 3$, calculations were also performed for $j \leq 2$. Figure 2.7 shows a comparison of both calculations for the kinematic configuration corresponding to the central values of the LQ kinematic setting in this experiment. The average difference is around 6% and never exceeds 12%. It is expected that the inclusion of higher angular momentum components will change the cross section by less than this amount. Therefore, in this experiment only those NN force components were used for which the angular momentum j of the NN system was not larger than three.

Also the final state is expanded in partial waves with total three-body angular momentum J. The calculations performed for this experiment include contribu-
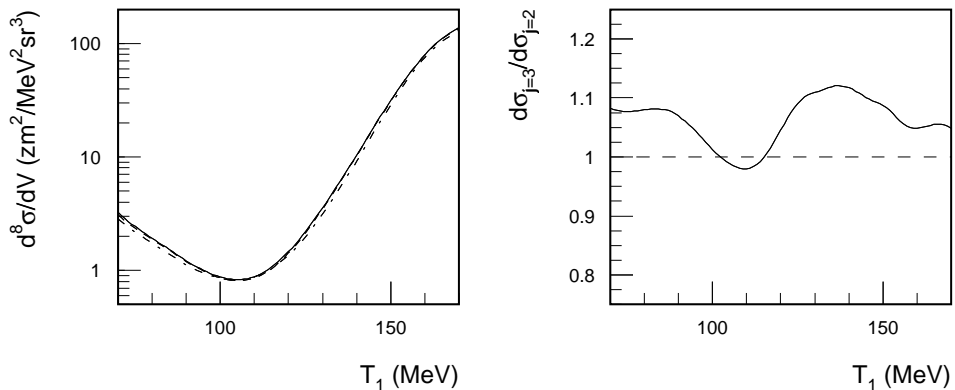
Figure 2.7: *Comparison of cross sections calculated by Golak et al. taking into account a different number of NN force components. In the left panel, the dot-dashed and solid curves correspond to calculations including force components with $j \leq 2$ and $j \leq 3$, respectively. The kinematic conditions correspond to the central values of LQ: $(\omega, q) = (220\ MeV, 305\ MeV/c)$, $\theta_1 = 55°$ and $\theta_2 = -105°$.*

tions up to $J = \frac{19}{2}$, which – within the kinematic domain of this experiment – ensures convergence to better than 2% on average .

Uniqueness of kinematic configurations

The kinematic configuration is not necessarily uniquely defined for a given electron kinematic setting (ω, q) and a set of values $(\theta_1, \phi_1, \theta_2, \phi_2, T_1)$ for the two outgoing protons. Figure 2.8 shows the kinematically determined curve for a selected angular combination. Here, for T_2 two possible solutions exist for $T_1 > 170$ MeV. Not only does this lead to ambiguities in the calculated cross section, it also introduces a mathematical singularity in the phase space factor (defined in Eq. 2.4) at the point corresponding to the maximal T_1 value. In this experiment, this kind of ambiguities is not relevant as the lowest detectable proton energy for the backward proton T_2 is 48 MeV.
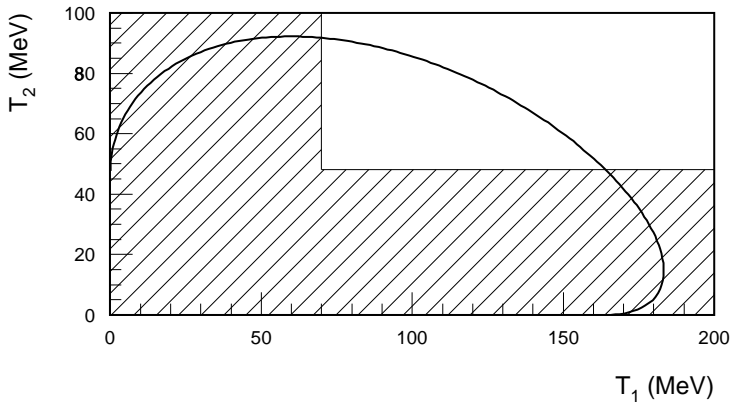
Figure 2.8: *Kinematically determined curve in the (T_1, T_2) plane for a fixed electron kinematic setting and fixed angles for the two outgoing protons. The curve shown corresponds to the central configuration of LQ, i.e., $\theta_1=55°$, $\theta_2=-105°$. The hatched area is not covered by the experimental detection volume.*

Averaging over the experimental detection volume

As mentioned, the theoretical cross section depends on seven kinematic variables that uniquely define the configuration. In general, the data are presented as a function of two or three quantities, derived from the basic kinematic variables. In this way an implicit averaging over the other quantities within the experimental detection volume is performed.

For a fair comparison between theory and data, the same averaging should be applied to the calculated cross sections. This averaging cannot be performed analytically because of the complexity of the integration limits, *i.e.*, the shape of the experimental detection volume. Performing the necessary integration by a Monte-Carlo method (*c.f.* section 4.4) requires too many computational resources to be performed with sufficient accuracy within a reasonable amount of time. Therefore, the integrals were approximated by a sum over an orthogonal grid.

The averaging of the cross section over the experimental detection volume was performed for the central value of (ω, q) only, because of constraints on
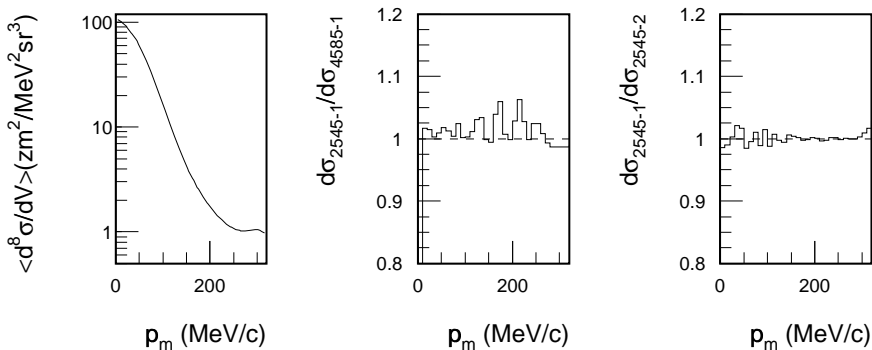
Figure 2.9: *Theoretical cross section for the LQ kinematic setting as a function of the neutron momentum, averaged over the experimental detection volume. The left panel shows the calculated cross section, the middle and right-hand panels show the ratio of the cross section calculated with the finest grid to two coarser grids. The numeric labels in these two panels specify the grid spacing. $d\sigma_{ijkl-m}$ indicates $\Delta\theta_1=i°$, $\Delta\phi_1=j°$, $\Delta\theta_2=k°$, $\Delta\phi_2=l°$, and $\Delta T_1=m$ MeV.*

the available computational resources[†]. The dependence of the cross section on the electron variables was investigated by comparing the calculated results for the various kinematic configurations measured. The dependence on ω is close to linear, which implies that no change in cross section is induced by taking the central value for (ω, q). The q-dependence of the cross section shows an exponential decay (see section 5.4), which implies that the weighted average of the data corresponds to a smaller q value than the one used to calculate the cross section. This effect introduces a systematic underestimation of the cross section by at most 6%, as determined from the q dependence at low p_m.

For a given interval in the variables in which the cross section is presented, *e.g.*, an interval Δp_m, the average cross section is defined as

$$\left\langle \frac{d^8\sigma}{dV} \right\rangle (\Delta p_m) = \frac{\int \frac{d^8\sigma}{dV}(\boldsymbol{v}) D(p_m(\boldsymbol{v}); \Delta p_m) D(\boldsymbol{v}; \boldsymbol{A}) d\boldsymbol{v}}{\int D(p_m(\boldsymbol{v}); \Delta p_m) D(\boldsymbol{v}; \boldsymbol{A}) d\boldsymbol{v}}, \qquad (2.11)$$

[†]Calculation of the half-shell amplitudes $|p_{rel}p_{cm}\alpha\rangle$ with NN force components upto $j = 3$ and a current operator that includes MECs takes approximately 15000 CPU seconds on a Cray C916/121024 supercomputer.
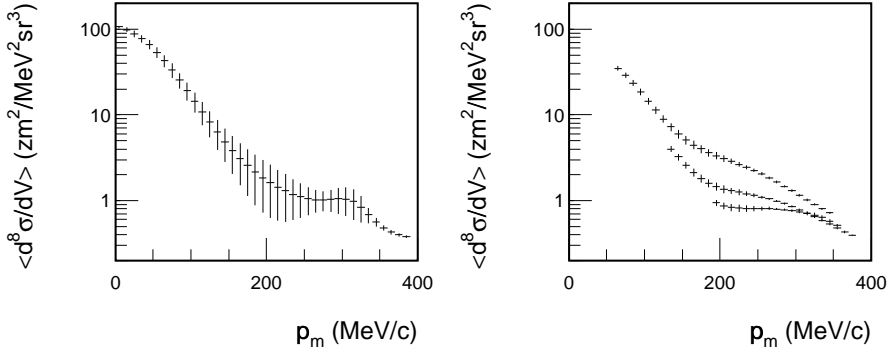
Figure 2.10: *Average cross section as a function of the missing momentum for the LQ kinematic setting. The left-hand panel is averaged over the entire detection volume without additional constraints, whereas in the right-hand panel the momentum difference p_{13} was limited to slices of 50 MeV/c wide, centred around 475, 375, and 275 MeV/c (in top-to-bottom order). Error bars indicate the width of the contributing cross section distribution.*

where $\boldsymbol{v}$ is the vector of laboratory quantities $(\theta_1, \phi_1, \theta_2, \phi_2, T_1)$, $\boldsymbol{A}$ is the acceptance region of the experimental detection setup and $D(\boldsymbol{x}; \boldsymbol{R})$ is a two-valued function that is only different from zero if $\boldsymbol{x}$ is inside the region $\boldsymbol{R}$.

The two integrals are approximated by their sums, determined with equidistant, orthogonal grids in the laboratory quantities $\boldsymbol{v}$. The distance between the gridpoints was chosen in such a way that the approximation errors introduced in the final result are below 6%, *i.e.*, comparable to the intrinsic uncertainty of the calculations due to the partial wave truncation. To verify the accuracy obtained, the cross section was calculated with a varying amount of grid points; the results of these calculations are displayed in Fig. 2.9. From these and similar tests it was concluded that a grid point density of $(\Delta\theta_1, \Delta\phi_1, \Delta\theta_2, \Delta\phi_2, \Delta T_1) = (2°, 5°, 4°, 5°, 1 \text{ MeV})$ is sufficiently accurate[‡].

[‡]This requirement on the grid density leads to about 2.5×10^6 points per kinematic setting. Calculation of one grid point typically takes about 0.6 seconds on a 270 MHz UltraSPARC–IIi processor, which implies that it takes about 17.5 CPU days to calculate the grid for one kinematic setting and one current operator.

The averaging of the cross section over the experimental detection volume may obscure dependencies of the cross section on non-explicit variables. Such dependencies lead to a large spread in the values for the individual cross sections contributing to a certain grid point. To investigate such dependencies, the standard deviation of the cross section distribution from which the average is derived was determined for every bin.

Figure 2.10 shows the missing-momentum distribution for the LQ kinematic setting. In the left-hand panel, no limitations were imposed on the contributing part of the detection volume. From the observed spread, which is as large as 60% around 200 MeV/c, it can be concluded that the cross section depends strongly on a non-explicit variable. In the case shown, the dependence on the momentum difference p_{13} is relatively strong, as the experimental acceptance contains an 'FSI configuration' around p_m=300 MeV/c. Moreover, the detection volume in the (p_m, p_{13}) plane is triangular in shape in such a way that for higher p_m values, increasingly lower values of p_{13} are covered. A projection on p_m for slices in p_{13} of 50 MeV/c wide shows that the spread of the theoretical distribution is reduced to less than 10%, as shown in the right-hand panel.

Considerations regarding relativity

At present, no framework exists to solve the three-body problem in a Lorentz-covariant manner. Although certain parts of the calculations – especially the kinematics and the calculation of the phase-space factor – can be performed with 'relativistic' kinematics, this would introduce internal inconsistencies in the calculation, as the wavefunctions and operators are entirely non-relativistic. By performing the theoretical calculations in a completely non-relativistic fashion, these inconsistencies can be avoided, although at the cost of introducing kinematic ambiguities.

In comparing calculations to data, the momenta that are explicitly shown along the axes are kept identical, *e.g.*, in presenting a missing-momentum distribution, the theoretical cross section shown for a particular value of p_m corresponds to the same momentum being used for p_3 in the calculation. This implies at the same time that the coverage of the non-explicit momenta (in this case p_1 and p_2) contributing to the average cross section is slightly different from the one spanned in the experiment.
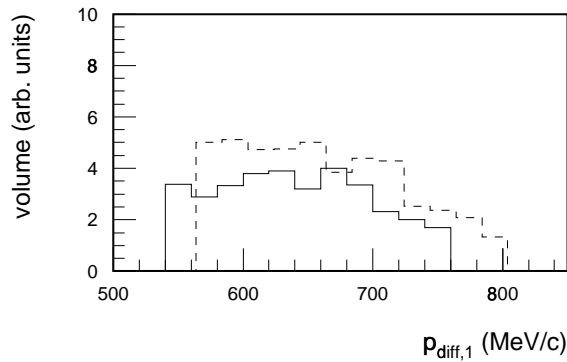
Figure 2.11: *Range in $p_{diff,1}$ contributing to the region $p_m < 100$ MeV/c. The solid (dashed) curve shows the distribution according to a non-relativistic (relativistic) calculation of the kinematics. The effective $p_{diff,1}$ value in the non-relativistic case is approximately 20 MeV/c too low. (kinematic configuration: LQ)*

The effect of this momentum mismatch was investigated for various kinematic conditions. The largest discrepancies were observed in the low p_m region, as this domain is covered primarily by p_1 values around 540 MeV/c. As the cross section shows a sizeable dependence on $p_{diff,1}$, the mismatch introduced in $p_{diff,1}$ is expected to be the most significant factor.

For the kinematics LQ at $p_m < 100$ MeV/c, the domain of $p_{diff,1}$ contributing to the cross section is shown in Fig. 2.11. The momentum mismatch of $p_{diff,1}$ amounts to 20 MeV/c. From the dependence of the cross section on $p_{diff,1}$, the expected change in the theoretical cross section due to this mismatch is estimated to be around 8%.